Pulsed laser deposition synthesis of high entropy carbide (HfNbTaTiZr)C thin films with near-equiatomic composition

T. N. Hogenelst

August 4th, 2021

Abstract

The high entropy carbide (HfNbTaTiZr)C is a material predicted to have excellent thermal and mechanical stability and has been reported to possess good anti-wear and frictional properties. Existing studies on (HfNbTaTiZr)C have focused predominantly on bulk properties. In this thesis pulsed laser deposition was used to grow (HfNbTaTiZr)C thin films on Si(100) and Al_2O_3(0001) from a stoichiometric target consisting of HfC, NbC, TaC, TiC and ZrC. Deposition parameters were optimized for near-equiatomic surface composition of metals and carbon, measured by X-ray photoelectron spectroscopy. The effects of deposition fluence (6-8, 7-14 J/cm^2) and process gas pressure (10^{-2} mbar $-$ 10^{-1} mbar) on surface composition were studied. A trend of increasing Nb and Ta concentration at higher deposition fluence was found. Furthermore a trend of decreasing concentration of lighter metals Ti, Zr, and Nb at higher deposition pressures was found. The results are explained through ablation threshold difference, preferential scattering and substrate resputtering. X-ray diffraction on (HfNbTaTiZr)C grown on Si(100) and Al_2O_3(0001) confirm successful growth of polycrystalline rock salt (HfNbTaTiZr)C by pulsed laser deposition. A difference in peak broadening of x-ray diffraction spectra from Si- and Al_2O_3-deposited films indicates a difference in grain size between deposition substrates. In conclusion, stoichiometric transfer in pulsed laser deposition of a multi-elemental HfC:NbC:TaC:TiC:ZrC target is discussed and a future outlook is provided on relevant experiments on (HfNbTaTiZr)C thin films.

Keywords: high entropy carbide, thin films, pulsed laser deposition, X-ray photoelectron spectroscopy, X-ray diffraction, rock salt

Contents

Acknowledgements

This thesis was written during an internship position at the Advanced Research Center for Nanolithography (ARCNL) within the Materials and Surface Science for EUV Lithography group (MatSurf). A collaboration was established with the ARCNL Contact Dynamics group for future characterisation methods (nanoindentation, atomic force microscopy). Frequent discussions about the theoretical framework were facilitated by members of the Univeristy of Amsterdam, van der Waals-Zeeman Institute for Experimental Physics (WZI). Much of the work that was performed would not have been possible without the support of the following people:

ARCNL
Dr. Roland Bliem (group leader MatSurf, thesis supervisor)
For many insightful discussions, guidance and support throughout the duration of the project

Alessandro Troglia (PhD student MatSurf)
Stefan van Vliet (PhD student MatSurf)
For support regarding experimental and analytical skills relevant to vacuum physics and surface analysis, and for performing XPS and XRD measurements on (HfNbTaTiZr)C

Cyrian Leriche (PhD student Contact Dynamics)
For collaboration on initial nanoindentation measurements

University of Amsterdam, WZI
Dr. Katerina Newell (Assistant-professor WZI)
For facilitating the theoretical framework regarding density functional theory (DFT) of high entropy materials

Corentin Morice (Postdoctoral student WZI)
For facilitating lectures and discussions on DFT

Bram van der Linden (MSc student WZI)
For discussions on properties of (HfNbTaTiZr)C calculated with DFT

1 Introduction

Extreme thermal, chemical and frictional conditions are required for many existing technological processes. Maintaining such conditions requires materials that can withstand them. Improving the ability of materials to operate in extreme conditions allows for development of new technology. The process of alloying has been central to the development of materials with properties required for operating under increasingly intense conditions. The primary alloying strategy for modern materials has been conventional (super)alloying, which is based on the addition of small quantities of secondary material to one (or more) primary material(s) [1]. On the contrary, the strategy of equiatomic multicomponent alloying is based on mixing components in equiatomic ratios, and has found application only recently compared to conventional alloying and superalloying. In 2004, Cantor *et al.* have shown that the equiatomic multicomponent alloy $Fe_{20}Cr_{20}Mn_{20}Ni_{20}Co_{20}$ forms a single-phase fcc solid solution, whereas for many multicomponent alloys discovered at that time, a tendency exists to form multi-phase structures [1]. In the same year, Yeh *et al.* introduced configurational entropy as an explanation for the tendency of equiatomic 5-component alloys to form a solid solution structure, coining the term high entropy alloy (HEA) [2]. In several cases HEAs have shown augmented material properties as compared to conventional alloys [1, 2, 3].

The presence of the high entropy solid solution phase is not unique to equiatomic multicomponent alloys, and also occurs in equiatomic multicomponent oxides, carbides, borides, and nitrides, grouped under the term high entropy ceramics (HECs) [4, 5]. The relevance of HECs stems from that conventional ceramics already contain many materials capable of withstanding extreme conditions. In particular, refractory metal carbides are applied in operating conditions where thermal stability, high hardness and chemical inertness are required [6]. Improving properties of refractory materials has a clear technological relevance for coating materials, which explains the interest in high entropy metal carbides (HERMCs). It has been shown that HERMCs can possess lower thermal conductivity [7, 8] and higher hardness [9, 10, 11] as compared to binary refractory metal carbides. In some cases HERMCs show better frictional and wear properties compared to binary refractory carbides [12, 13, 14]. Owing to these augmented material properties, HERMCs are thought to be excellent coating materials for extreme thermal and frictional conditions. Furthermore, HERMC coatings have been studied in the context of *in vitro* biomedical applications for cell adhesion [13, 15, 16].

The compositional space of HERMCs contains many potential materials for applications with technological relevance. In this thesis, (HfNbTaTiZr)C is chosen as the high entropy refractory metal carbide of interest. The aims of this study are to identify a reproducible recipe for pulsed laser deposition (PLD) synthesis of (HfNbTaTiZr)C thin films and to characterize the resulting films in terms of composition and crystallinity. Two factors weigh into the specific choice of (HfNbTaTiZr)C. Firstly the choice is based on the entropy formation ability (EFA) formalism of Sarker *et al.* [9], which predicts synthesizability of an n-species system from first principles calculations. From the materials assessed in the study of Sarker *et al.*, (HfNbTaTiZr)C has the second highest predicted EFA[1]. Furthermore, x-ray diffraction (XRD) results of HERMC thin films synthesized by spark plasma sintering indicate polycrystalline rock salt (HfNbTaTiZr)C [9]. The second factor is that (HfC:NbC:TaC:TiC:ZrC) PLD targets with equiatomic composition are commercially available.

[1] Within the EFA formalism of Sarker *et al.*, entropy content of a compound is described by the EFA descriptor, defined as '*the inverse of the standard deviation of the energy distribution spectrum of metastable compound configurations above the zero-temperature ground state of the compound*' [9].

The preferred crystal structures of the deposited samples are amorphous or rock salt solid solution (HfNbTaTiZr)C. The surface composition of PLD-synthesized (HfNbTaTiZr)C thin films is measured by x-ray photoelectron spectroscopy (XPS). Process parameters of the PLD setup are varied until a near-equiatomic surface composition is achieved. The requirement of near-equiatomicity is set in order to maximize configurational entropy present within the system, favouring the proposed high entropy nature of the (HfNbTaTiZr)C rock salt phase. To confirm whether or not amorphous and crystalline growth can be achieved within the PLD process parameter space considered in this thesis, the resulting films are analysed with x-ray diffraction (XRD). Details of the surface compositional analysis, optimization procedure and XRD methods are outlined in section 3. For cases where a recipe successfully produces rock salt (HfNbTaTiZr)C, grain size of the resulting rock salt films are estimated from the Scherrer equation. Furthermore a difference between ambient oxidation behaviour of near-equiatomic (HfNbTaTiZr)C thin films deposited on Si(100) and Al_2O_3(0001) is reported. An overview of the results can be found in section 4. The results, as well as the performance of PLD for synthesis of high entropy refractory metal carbides are discussed in section 5, and the discussion is followed by an outlook on relevant future experiments.

2 Literature Review

2.1 high entropy materials

High entropy materials are thought to follow an unique mechanism through which a stable crystal structure consisting of all elements is formed, as opposed many individual patches of alloys. The crystal structure is formed under the circumstance that configurational entropy is dominant in the system free energy, which determines the (meta)stable phases of the system.

A phase with a lower free energy is on average more likely to form. As an example of the role of configurational entropy, consider the Gibbs free energy of a system, given by:

$$G = H - TS, \tag{1}$$

where H is the system enthalpy, T is temperature, and S is the system entropy. High entropy materials are materials that have an increased configurational entropy, which stems from intermixing n elements in equiatomic concentration. The configurational entropy is defined as:

$$S = -R \sum_{i=1}^{n} c_i \ln(c_i), \tag{2}$$

under the condition that the total concentration be normalized:

$$\sum_{i}^{n} c_i = 1. \tag{3}$$

For an equiatomic n-component system, $c_i = c = \frac{1}{n}$, and the configurational entropy for an equiatomic n-component $S^{(n)}$ can be rewritten as:

$$S^{(n)} = -R\Big(c_1 \ln(c_1) + \cdots + c_n \ln(c_n)\Big) = -R\Big(cn \ln(c)\Big) = -R \ln\left(\frac{1}{n}\right) = R \ln n, \tag{4}$$

which increases with increasing n.

For some high entropy materials it has been reported that these materials possess properties which are beyond the best properties of their constituents. In terms of composition, Yeh et al. [2] have defined an empirical rule of 5 to 35% mutual concentration of elements in case of high entropy alloys. For high entropy refractory metal carbides such a rule is not known. It is however expected that the possible concentrations of metal carbides that allow for a high entropy structure lies within some range comparable to that of the high entropy alloys.

2.2 Pulsed laser deposition as a synthesis method for equiatomic (HfNbTaTiZrC) thin films

(HfNbTaTiZr)C has been synthesized previously by spark plasma sintering [9, 10, 17, 18], hot-pressed sintering [19, 20], radio frequency (RF) sputtering [21], co-sputtering [12, 13], conventional magnetron sputtering [16] and high-power impulse magnetron sputtering [22]. Table 1 shows an overview of film thickness of (HfNbTaTiZr)C synthesized by various existing methods considered in literature. The majority of existing literature concerns (HfNbTaTiZr)C with μm- or mm-range film thickness. Despite the capability of most methods mentioned in table 1 to produce thin films, past literature have predominantly focused on bulk properties of (HfNbTaTiZr)C.

PLD-synthesized (HfNbTaTiZr)C thin films have not yet been reported in literature. They are of interest because of the following two reasons. Firstly, it is known that varying PLD process parameters such as deposition pressure [23, 24], deposition fluence [25], and process gas composition [26] allows for variation in the composition and structure of deposited samples. The ability to vary composition of deposited samples through PLD process parameters provides a pathway towards achieving the (near-)equiatomicity required for the high entropy solid solution phase. Secondly, a large body of literature exists on composition, structure, and surface properties of PLD-synthesized binary refractory metal carbide thin films [27, 28, 29, 30, 31, 32, 33, 34]. Synthesis of (HfNbTaTiZr)C thin films with PLD allows for straightforward comparison between film properties of PLD-synthesized binary carbides and high entropy carbides.

Substrate	**Synthesis Method**	**Thickness**	**Reference**
n.a.	Spark Plasma Sintering	$\sim$ mm	[7]
n.a.	Hot Pressing	$\sim$ mm	[20]
316-L	Magnetron Sputtering	1.5 μm	[16]
n.a.	High-temperature Sintering	n.a.	[8]
C45	Co-sputtering	2 μm	[12]
M2	Co-sputtering	2 μm	[12]
Ti6Al4V	Co-sputtering	2 μm	[13]
Ti6Al4V	Co-sputtering	2 μm	[13]
n.a.	High-power impulse magnetron sputtering	300 nm	[22]
Al_2O_3	RF sputtering	100 nm	[21]

Table 1: Overview of deposition substrates, synthesis method, and thickness of (HfNbTaTiZr)C high entropy carbide produced by existing synthesis methods.

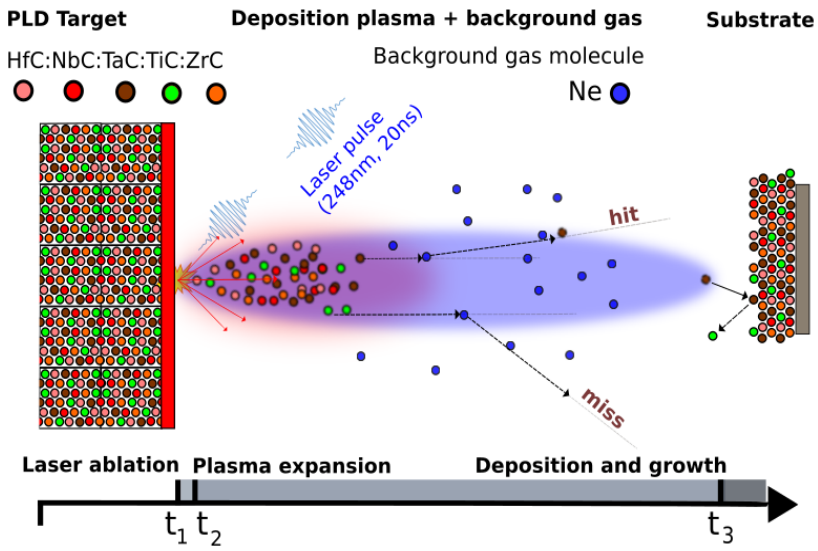

Figure 1: A schematic representation of the PLD process of (HfNbTaTiZr)C. Target material is ablated by laser pulses (KrF, 248nm, 20ns). As a consequence of the high laser intensity, a plasma is formed. The plasma expands towards a deposition substrate and will scatter off process gas molecules during the expansion. Eventually the constituents of the deposition plasma will reach the deposition substrate.

2.3 Physical considerations for PLD of multi-elemental carbides

In pulsed laser deposition, a pellet of the material of interest, the PLD target, is irradiated by high-intensity laser pulses in order to achieve local vaporisation and plasma formation (ablation). Two main regimes exist w.r.t. the intensity of the incident laser light. At low intensities, below the plasma ignition treshold, laser pulses do not provide enough energy to ablate target material. In this regime, heating, melting, and vaporisation of target material occurs [35]. At intensities above the plasma ignition threshold, an ablation plasma will form in addition to the phenomena that occur below the plasma ignition threshold [35]. Pulsed laser deposition uses laser intensities above the plasma ignition treshold and the resulting plasma is used as the main source of material for deposition. A concise description of the PLD process is thus that the absorbed laser energy results in material removal in the form of a plasma plume that expands away from the target. The material is collected by a substrate at a fixed target-to-substrate distance $d_{T-S} = 55mm$. It is useful to subdivide the process into three regimes: laser ablation of PLD target material, plasma expansion of ablated material, and collection of deposition plasma by the deposition substrate. Figure 1 shows a schematic representation of the process.

A complete description of the deposition process of is beyond the scope of this thesis. Instead, selected topics are introduced in the following sections: laser ablation (sec. 2.3.1 - 2.3.3) and process gas pressure effects (sec. 2.3.4).

2.3.1 The two-temperature model for pulsed laser ablation

The ablation process of target material depends on laser intensity, pulse length, and laser wavelength [35]. The dependence on pulse length and laser wavelength can be ignored since these parameters are determined by the PLD system. Here, an intensity-dependent model for pulsed laser ablation of

a single material is introduced, conform to ref. [35]. The consequences of having a multi-elemental PLD target are discussed in 2.3.3.

The model assumes that the dominant energy transfer mechanism in PLD occurs through electron-phonon interactions. It is described in terms of a two-temperature model of electronic and phononic lattices. In case of a single material, and laser intensity below the plasma ignition threshold, the model can be cast into a one-dimensional, two-temperature diffusion model [35]:

$$C_e \frac{\partial T_e}{\partial t} = \frac{\partial}{\partial z}(k_e \frac{\partial T_e}{\partial z}) - \Gamma_{e-p}(T_e - T) + S(z,t) \tag{5}$$

and,

$$C \frac{\partial T}{\partial t} = \Gamma_{e-p}(T_e - T), \tag{6}$$

with T_e and T the electron and phonon temperature at a time t. C_e and C are the heat capacities per unit volume of electrons and phonons, respectively; k_e is the non-equilibrium electron thermal conductivity; Γ_{e-p} is the electron-phonon coupling constant, and $S(z,t)$ the heat source term. In equation 5, the non-equilibrium electron thermal conductivity is expressed in the equilibrium thermal conductivity of a metal, $k_0(T)$ [35]:

$$k_e = k_0(T) \cdot \frac{T_e}{T}. \tag{7}$$

The system of interest is the PLD target, and the source term $S(z,t)$ represents the energy influx into the the target material caused by absorption of laser energy. Generally the source term has to take into account the loss caused by reflectivity as $S \propto (1-R)$. The source term should further represent the process of absorbing laser energy and therefore takes into account the absorption coefficient of a material. An intensity depth profile $I(z) \propto e^{-\alpha z}$ is assumed, in accordance with the Beer-Lambert law, where α is the absorption coefficient of the material. The source term $S(z,t)$ in equation 5 can thus be rewritten as [35]:

$$C_e \frac{\partial T_e}{\partial t} = \frac{\partial}{\partial z}(k_e \frac{\partial T_e}{\partial z}) - \Gamma_{e-p}(T_e - T) + (1-R)\alpha I(t) e^{-\alpha z}. \tag{8}$$

In writing the absorption process according to the Beer-Lambert law, it must been assumed that the heat diffusion length into the PLD target material, l_T, is much smaller than both the dimensions of the laser beam on the target and the thickness of the PLD target [35]. In the regime of nanosecond laser pulses, the heat diffusion length can be approximated as [35, 36]:

$$l_T \approx \sqrt{2D\tau_p}, \tag{9}$$

with τ_p the laser pulse length, and D the heat diffusion coefficient:

$$D = \frac{k}{\rho c} \tag{10}$$

with k thermal conductivity, ρ density, and c specific heat capacity. The required parameters to calculate the heat diffusion length in metal carbides are well-documented in literature [37], allowing for an estimation of the accuracy of the thermal model for a given material.

In case the pulse energy exceeds the plasma ignition threshold, a plasma will be present. If the laser pulse is long enough to irradiate the plasma, laser-plasma interactions have to be taken into account. This can be achieved by modifying the source term in the two-temperature model [35]:

$$S(z,t) = (1-R)\alpha I(z,t) e^{-\int_0^t \alpha_{pl}\ v_{pl}\ dt} \tag{11}$$

where the intensity profile $I(z,t)$ is multiplied with an exponential attenuation factor that represents the laser intensity absorbed by the plasma. The amount of attenuation due to plasma absorption is calculated by integrating the product of plasma absorption coefficient α_{pl} and the hydrodynamic velocity v_{pl} over the pulse duration $t = \tau_p$.

2.3.2 The two-temperature model in the nanosecond pulse length regime

The interaction of laser energy and target material below and above the ignition threshold of the plasma both depend on the temporal profile of the laser pulse $I(t)$. More importantly, in equation 5 it has been assumed that the change in temperature is caused by electron-phonon interactions. In case of nanosecond laser pulses, the interaction time scale of electron-phonon interactions is many orders of magnitude smaller than the pulse length, and it is assumed that the electronic and phononic lattices are in thermal equilibrium over the entire pulse length τ_p [35].

In case of ablation below plasma ignition threshold, the nanosecond laser pulse time causes the two-temperature model to reduce to a simpler heat equation by setting $T = T_e$, leading to [35]:

$$C\frac{\partial T}{\partial t} = \frac{\partial}{\partial z}(k\frac{\partial T}{\partial z}) + (1-R)\alpha I(z,t)e^{-\alpha z}. \tag{12}$$

2.3.3 Considerations for nanosecond ablation of multi-elemental carbide tagets

Predictions from the two-temperature model for nanosecond laser ablation show reasonable agreement with experimental results in literature [35]. Variants of the model have been introduced for single metals [25, 38, 39], multi-elemental metal alloys [40, 41] and complex oxides [42, 43]. However, models for multi-elemental carbides have not been considered in literature. A possible explanation is that compared to metals and metal oxides, metal carbides require a large amount of energy per unit area before completely ablating. This is due to the high thermal stability of metal carbides, caused by a combination of high melting points, heat capacities and heat diffusivity of metal carbides. For ablation of equiatomic multicomponent metal oxides [25, 38] it is common to use a fluence close to 2 J/cm^2. For comparison, ablation of the refractory metal carbide ZrC requires a fluence above 5 J/cm^2 [32, 33, 34].

In general, the presence of multiple materials on the PLD target gives rise to a difference in the absorption process of laser energy. This can be seen through equation 12, which, for the case of ablation of a multi-elemental target consisting of grains, would contain multiple heat equation coefficients C_i, k_i, as well as multiple reflectivities R_i and absorption coefficients α_i in the source term $S(z,t)$. An alternative approach in the case of a multi-elemental target would be to replace the coefficients in the heat equation with average values $\tilde{C}, \tilde{k}, \tilde{R}$, and $\tilde{\alpha}$. Additionally, above the plasma ignition threshold, both the absorption properties of the plasma constituents and the hydrodynamic velocity at which they expand from the target surface may vary, represented by having various $\alpha_{pl,i}$ and $v_{pl,i}$ in equation 11.

2.3.4 Deposition pressure effects

After material is ablated by a laser pulse, it will expand into the PLD chamber vacuum in the form of a plasma. The plasma constituents interact with process gas through scattering. By varying the deposition pressure and the gas type, the scattering probability of plasma constituents and process gas atoms can be affected. Typically in PLD, the deposition rate at the substrate decreases with increasing process gas pressure. This is explained through the concept of mean free path λ_{mfp}. The mean free path is the average distance traveled by an atom before a collision with a gas molecule occurs. From kinetic theory of gases the mean free path in vacuum can be expressed as [44]:

$$\lambda_{mfp} \propto \frac{1}{p\sigma^2}, \tag{13}$$

with σ the scattering cross section, and p the pressure. Equation 13 shows that mean free path is inversely proportional to the product of pressure and the square of scattering cross section.

Experimental results of PLD on iron (Fe) and silver (Ag) show that deposition rate decreases as a function of increasing pressure up to about 10^{-2} mbar [23, 24]. For pressures around and above the order of 10^{-2} mbar, deviations from the expected pressure dependence occur for Ag in the form of multiple peaks in the deposition rate. The results of Fe shows no such features [23, 24]. Such an imbalance in deposition rate between elements present in deposition of (HfNbTaTiZr)C is not well-documented.

In the case that (HfNbTaTiZr)C ablation occurs above the fluence threshold of the elemental carbides, the plasma will contain Hf, Nb, Ta, Ti, Zr and C atoms. From hard sphere scattering theory the scattering angle is inversely proportional to scattering mass, so that particles with larger mass have a smaller average outgoing scattering angle [45]. All metal atoms are heavier than Argon (Ar) and Neon (Ne), and will have a forward scattering solution [45]. The mass difference between the metal ions translates in a lower probability for lighter metals to reach the deposition substrate after a scattering event. Carbon is lighter than both Ne and Ar, and therefore has a very low probability of forward scattering [45]. Because of this effect, it is expected that the choice of process gas (Ar or Ne) strongly affects carbon content.

In addition to the pressure dependence of the mean free path, the scattering cross section σ in equation 13 affects the probability for a collision to occur. Firstly, the static scattering cross section σ differs between the elements that are present in the deposition plasma ($\sigma = \sigma_i$). This will cause a different scattering probability for the individual elements. Secondly, the scattering cross section is dependent on particle kinetic energy ($\sigma = \sigma(E)$) [45]. Energy-dependent scattering cross sections $\sigma_i(E_i)$ for each element introduce complex variations in the deposition rate of multi-elemental material.

2.4 Surface roughening, substrate resputtering and melt ejection

Further processes that affect stoichiometric transfer in PLD are surface roughening of the PLD target, melt ejection from the PLD target and resputtering of deposited atoms at the deposition substrate. Melt ejection changes the stoichiometry of resolidified PLD target material.

Surface roughening of the PLD target occurs because the absorption process locally changes the PLD target surface. As a consequence of absorbing laser energy, the PLD target surface will locally remove material in the form of a plasma as well as melting a large amount of material surrounding the laser spot. The leftover material that is not completely ablated will be left behind on the PLD target surface as a melt pool. In between laser pulses, the melt pool re-solidifies.

Because not all materials on the target are ablated in equal proportions, the melt pool will be off-stoichiometric. The compositional imbalance introduces segregation of target material and therefore a difference in surface energy. Re-solidification contributes to surface roughening through that the off-stoichiometric melt pool will recrystallize in a three-dimensional structure as opposed to a flat surface [35]. Through this mechanism surface roughening alters the absorption properties and ablation conditions of the PLD target surface.

Resputtering is an effect that occurs in single-material and multi-elemental PLD due to that a fraction of ions in the deposition plasma has a large enough average kinetic energy to remove a deposited atom from the deposition substrate. Resputtering in multi-elemental PLD is expected to affect predominantly the concentration of lighter elements.

3 Methods

Pulsed laser deposition (PLD) was used for growth of (HfNbTaTiZr)C thin films on Si(100) and Al_2O_3(0001). The PLD process parameters were varied in order to affect the composition of the deposited films. The deposited films were analysed for surface composition by X-ray photoelectron spectroscopy (XPS). Initial experiments probing the relation between PLD process parameters and film composition have been performed. The knowledge from these experiments has allowed for directing the surface composition of PLD-synthesized HERMC thin films towards near-equiatomicity. Section 4 discusses the results of the optimization, and further discusses reproducibility and thickness calibration of the optimized PLD recipes. Recipes with near-equiatomic stoichiometry were analyzed with XRD to identify the crystal structure. For samples with polycrystalline XRD spectra, Scherrer analysis was performed order to extract peak positions and estimate particle size through peak broadening. The sections below introduce PLD, XPS and XRD.

3.1 Pulsed Laser Deposition

3.1.1 PLD optics and vacuum chamber

For synthesis of HERMC thin films, a commercial PLD setup was used provided by Twente Solid State Technology (TSST). A schematic of the PLD setup is provided in figure 2. A COMPEX 205F KrF excimer laser ($\lambda = 248$nm) provides nanosecond laser pulses ($\tau_p = 20$ ns, $f_R = 10$ Hz) with flat-top profile. The laser pulses are guided through a mask and focusing lens onto a piece of target material inside the PLD chamber. The fluence of the laser pulse at the PLD target is set by adjusting laser pulse energy, mask area, mask-lens distance d_{mask}, and lens-target distance d_{lens}.

The PLD chamber is evacuated by a multi-stage pumping system capable of ultra-high vacuum (UHV) pressures below 10^{-9} mbar. The laser is focused onto the PLD target through a quartz viewport which seals the UHV chamber. The viewport has a transmission coefficient T_1 of 0.912 at a wavelength of 248nm. The surface of the quartz viewport that faces the inside of the PLD chamber is polished regularly in order to restore transparency, which drops over time due to deposition of ablated material. The PLD chamber is further equipped with a second quartz viewport with a transmission coefficient $T_2 = 0.912$. A metal shutter avoids erroneous intensity measurements caused by a decrease of transparency due to deposition of ablated material.

The laser energy at the PLD target surface E_{dep} was calculated by accounting for the transmission coefficient of the second quartz viewport. Throughout depositions it was assumed that the transparency of the second quartz viewport remained unaffected, so that the deposition energy was calculated according to:

$$E_{dep} = \frac{1}{T_2} * E_{final} = \frac{1}{0.912} * E_{final} \ . \tag{14}$$

Measuring both the intensity at the PLD target and the laser spot area allows for calculation of the deposition fluence F (J/cm^2), which is defined as the total energy divided by the area onto which the energy is deposited:

$$F \equiv \frac{\{\text{total energy}\}}{\{\text{total area}\}} = \frac{E_{dep}}{A_{spot}} \ . \tag{15}$$

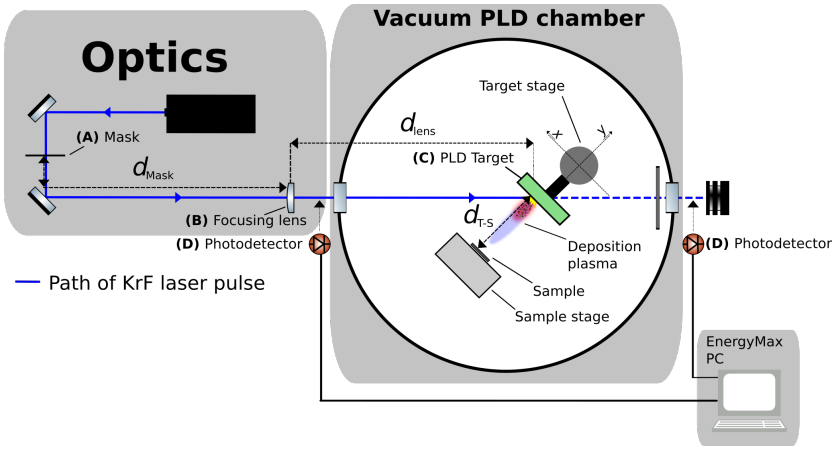

Figure 2: Schematic representation of the PLD setup. Main components outside the vacuum chamber that affect deposition fluence are the mask (A), which removes an undesired part of the spatial wavefront of the laser, and the focusing lens (B), which images the laser spot on the PLD target (C). The distance AB and BC determine the laser spot area. The laser energy before and after the PLD chamber is measured with a photodetector (D).

The beam spot area A_{spot} was measured by introducing a thin photoactive test target into the PLD chamber and irradiating it with the PLD laser at fixed laser parameters. The distance between focusing lens and quartz viewport was varied over a short range (mm) to produce laser spots on the test target with different focus. The test target was removed from the PLD chamber and the dimensions of the beam spot with best focus were measured with a caliper. The lens position that produces best focus was recorded and used for future depositions.

3.1.2 Sample preparation for UHV

Si(100) and Al_2O_3(0001) substrates were used for PLD of (HfNbTaTiZr)C. Substrates have to be prepared for UHV in order to avoid contamination. As-provided Si(100) substrates are covered with a protective polymer layer after mechanical cutting. To remove the protective layer, samples were cleaned by ultrasonication in acetone (10min), followed by IPA (10min). Al_2O_3(0001) substrates were cleaned by ultrasonication in IPA (10m). After ultrasonication the samples were mounted on flagpole-style sample plates with UHV-compatible double-sided carbon tape or conductive silver paint. Sample plates were then transferred to UHV via a loadlock.

3.1.3 PLD target and substrate stage

The PLD target consists of a hot-pressed HfC:NbC:TaC:TiC:ZrC pellet (equiatomic, 99.95% purity) and is attached to a target carousel. The target carousel can be translated in the x, y, and z-direction through a vacuum bellow. The deposition substrate is located on a sample stage which can be translated through a second vacuum bellow. An axisymmetric orientation between the center of the substrate and the laser spot on the PLD target was maintained throughout depositions. The target-substrate distance d_{T-S} is fixed at a value of 55mm. The substrate stage is equipped with a retractable shutter which can be closed such that deposition onto the substrate during target cleaning can be avoided.

3.1.4 Pre-ablation of target surface

Ablation of material in the nanosecond pulse length regime is dominated by thermal processes and therefore causes significant changes in the target surface. Examples are changes in surface roughness caused by crater formation around the ablation zone [35], and changes in local concentration caused by partial resolidification of molten material [35]. The target surface is further exposed to residual water and oxygen pressure in between depositions. It is therefore important to periodically re-prepare the target surface in a similar state as compared to previous depositions. This cleaning process is called pre-ablation and consists of performing laser ablation of the target surface while keeping the substrate stage shutter closed to avoid deposition. By moving the target stage in the plane of the laser spot, the laser spot is scanned over the target surface and thereby ablates material at a different location for every shot. The target surface is scanned over multiple times before starting a deposition in order to provide a target surface with similar roughness and composition. Pre-ablation was performed in the presence of process gas ($p \approx 4 * 10^{-2}$ mbar) in order to avoid deposition onto the laser viewport, which preserves its transmission coefficient.

3.1.5 Control of deposition pressure

The PLD chamber is connected to a gas cabinet equipped with Ar and Ne gas. This allows for Ne and Ar pressures during pre-ablation and deposition. A mass flow controller (MFC) valve provides a constant flow gas that enters the PLD chamber.

Deposition pressure was set by varying the conductance of a bypass line between the PLD chamber and a turbomolecular pump until a steady state between the gas in- and outflux at desired pressure is achieved. The total pressure p_T was measured by a full-range pressure gauge. The total pressure is the sum of all partial pressures, which in case of PLD depositions are the initial UHV pressure p_{init} and process gas pressure p_{proc}:

$$p_T = p_{init} + p_{proc} \tag{16}$$

In a UHV deposition no process gas pressure is present ($p_{proc} = 0$) so the total pressure is equal to the initial pressure:

$$p_{T,\mathrm{UHV}} = p_{init} + p_{proc} = p_{init} \tag{17}$$

For depositions in Ar or Ne, the process pressure is many orders of magnitude larger than the initial pressure ($p_{proc} \gg p_{init}$), and the total pressure is approximated as the process pressure:

$$p_{T,proc} = p_{init} + p_{proc} \approx p_{proc}. \tag{18}$$

3.1.6 Deposition process

A complete deposition cycle consists of sample preparation, selection of gas atmosphere and pressure, laser energy measurements, pre-ablative cleaning, and deposition. The relevant experimental parameters that are varied between depositions are summarized in table 2.

Parameter	Symbol	Units	Range
Deposition fluence	F_{dep}	$^{J}/_{cm^2}$	6 - 12
Laser discharge voltage	U_L	kV	19 - 27
Laser repetition frequency	f_R	Hz	10
Process gas pressure	p_{proc}	mbar	10^{-2} - 10^{-1}
Deposition time	t_{dep}	s	600 - 1800

Table 2: Overview of PLD process parameters that were varied in this thesis.

3.2 X-ray Photoelectron Spectroscopy

3.2.1 Measurement principle

X-ray photoelectron spectroscopy can be used to determine the surface composition of a solid. The technique relies on the interaction of soft x-rays (10 pm $< \lambda <$ 10 nm) with solid matter [46, 47]. In the setup for this thesis, x-rays are obtained by irradiating an aluminum anode with high-energy electrons, causing it to emit Aluminum-K$_\alpha$ (Al-K$_\alpha$) radiation. The x-rays are monochromated by a Ge mirror, resulting in narrow energy spectrum centered about a photon energy $h\nu$ of 1486.6 eV.

Upon reaching the sample surface, x-ray photons excite core level electrons of the atoms (*s-, p-, d-, f*-shell electrons) up to a finite depth. The atoms in the excitation volume start emitting photoelectrons with a kinetic energy according to the photoelectric effect [46]:

$$E_{kin} = h\nu - E_b - \phi_s, \tag{19}$$

where $h\nu$ is the energy of the x-rays used to excite the solid, the binding energy E_b is the energy difference between the electron core level and the vacuum level, and ϕ_s is the spectrometer work function [46]. Figure 3 shows a schematic representation of photoexcitation of electrons. In this thesis, the surface composition of (HfNbTaTiZr)C was calculated from Hf 4*d*, Ta 4*d*, Nb 3*d*, Zr 3*d*, Ti 2*p*, O 1*s* and C 1*s* transitions. These transitions are preferred because they vary the least in photoelectron kinetic energy, minimizing variations that are caused by the dependence of the XPS components on photoelectron kinetic energy. Photoelectrons are emitted from the sample surface into an energy-dispersive analyser and deflected by an electrostatic lens. The binding energy of photoelectrons is material-specific, hence the voltage over the deflection lens can be varied as to detect photoelectrons with a specific kinetic energy. An integrated spectrum of electron count as a function of kinetic energy is obtained by varying the voltage over the deflection lens. It is common to express the energy axis of the kinetic energy spectrum in terms of the electron binding energy:

$$E_b = h\nu - E_{kin} - \phi_s, \tag{20}$$

For Al-K$_\alpha$ radiation, elemental spectra and binding energies are well-documented through experimental measurements [46]. This allows for identification and quantification of elements that are present at the sample surface.

The spectrum measured in XPS is dominated by electrons stemming from the first few tens of Ångströms of the surface. This is caused by the lower mean free path of electrons compared to the mean free path of x-ray photons in solids [46]. The intensity of both photons and electrons at distance z in solids decays exponentially. The decay length is dependent on the mean free path λ in accordance with the Beer-Lambert law:

$$I(\lambda, z) \propto e^{-\frac{1}{\lambda}z}. \tag{21}$$

The difference in mean free path ($\lambda_e \ll \lambda_p$) causes photoelectrons that are excited by photons deeper within the excited volume to have a lower probability to escape the solid.

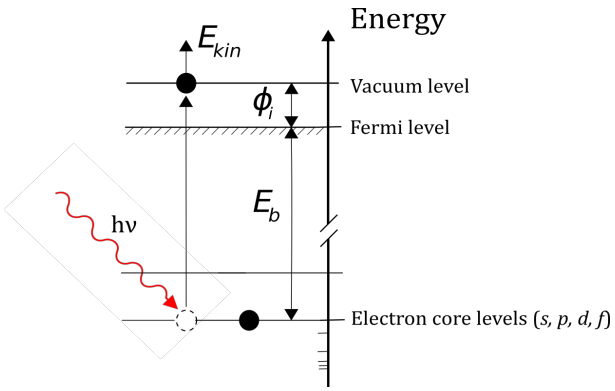

Figure 3: A schematic representation of the excitation of photoelectrons from core levels. An x-ray photon with energy $h\nu$ excites a core level electron to the Fermi level, which requires binding energy E_b. In order to promote the electrons from the Fermi level into vacuum an additional energy ϕ_i is required, which is the work function of the material. Electrons that are promoted to the vacuum level are no longer bound to the solid and propagate towards the analyser with the remaining kinetic energy E_{kin}.

3.2.2 Interpretation and quantitative analysis of XPS measurements

The first step towards quantitative analysis of XPS data is peak fitting and calculation of the peak area of the atomic transitions. Background subtraction is important for accurate determination of peak area in XPS. Not using appropriate background fitting causes under- or overestimation of peak areas. For all XPS data in this thesis a Shirley background was used to subtract background signal. After background subtraction, a peak shape may be fitted to the atomic transitions to determine the area of the peak. The peak shape of atomic transitions can contain both Lorentzian and Gaussian components [46]. For this reason a Voigt profile was used, which is the convolution of a Gaussian and Lorentzian profile.

Next to background subtraction and choice of peak profile, it is important for accurate fitting of XPS data to take into account the physics of exciting s-, p-,d- and f-transitions with x-ray photons. The p-,d- and f-transitions are known to exhibit two peaks with fixed energy difference and area ratio between the peak positions and areas. The change in peak position in p-, d-, and f-transitions is caused by a degeneracy in electron energy for spin-up and spin-down, which is lifted by the laser field. The lifting of degeneracy occurs through populating electrons with spin-up and spin-down into two accessible electronic states with different binding energies ΔE. The peak area ratio is fixed by the angular and spin quantum numbers l and s: $j = l + s$, with $s = \pm 1/2$ [47]. Table 3 shows the values of j and the area ratio of s-, p-, d-, and f-transitions.

Subshell	j	Area ratio
s	1/2	n/a
p	1/2; 3/2	1:2
d	3/2; 5/2	2:3
f	5/2; 7/2	3:4

Table 3: Overview of spin-orbit split area ratios of s-, p-, d-, and f-transitions which are used in XPS analysis.

A difference in material response to x-rays has not yet been discussed. The probability of an x-ray exciting a photoelectron towards a vacuum state depends on the photoionisation cross section, which differs between materials. Values for photoionisation cross sections are well-documented for a large range of x-ray energies, including the excitation energies common to XPS [48, 49]. The total peak area of an element-specific transition is divided by its transition-specific photoionisation cross section, resulting in the cross section-corrected peak area. The area of the individual cross-section corrected peaks can then be normalized to the sum of cross section-corrected peak area.

XPS can furthermore be used for chemical interpretation. Chemical sensitivity of XPS stems from a difference in peak position between possible chemical bonding states of a material [46]. A covalent bonding state will involve valence electrons, the absence of which causes a difference in electronic screening of the core levels of the material. This alters the photoelectron binding energy of a compound. An example is the difference in peak position of Ti $2p_{3/2}$, $2p_{1/2}$ (454.1 eV, 460.2 eV) and TiO_2 $2p_{3/2}$, $2p_{1/2}$ (458.8 eV, 464.3 eV) [46]. By comparing the peak area stemming from the Ti bonded with Ti to the Ti bonded with oxygen, a ratio of metal to metal oxide n can be calculated as:

$$n = \frac{\{\text{concentration of Ti metal}\}}{\{\text{concentration of Ti metal + concentration of Ti oxide}\}}. \tag{22}$$

Similarly the metal-to-metal concentration of interest is defined as:

$$n_M = \frac{M_i}{\sum_j M_j}, \tag{23}$$

where M_i is the concentration of the i-th metal, which is normalized to the sum of concentration of all metals. Another quantity of interest is the carbon-to-total metal ratio, defined as:

$$n_C = \frac{C}{C + \sum_j M_j}, \tag{24}$$

where C is the total amount of carbon and $\sum_j M_j$ is the total amount of metals.

3.3 X-ray Diffraction

3.3.1 Description of the methodology

X-ray diffraction is a technique that allows for identification of crystal structures. The technique measures the diffraction angles of incident light caused by interactions with the material. The diffraction angles of x-rays at a given wavelength are specific to the lattice spacing d of an ordered

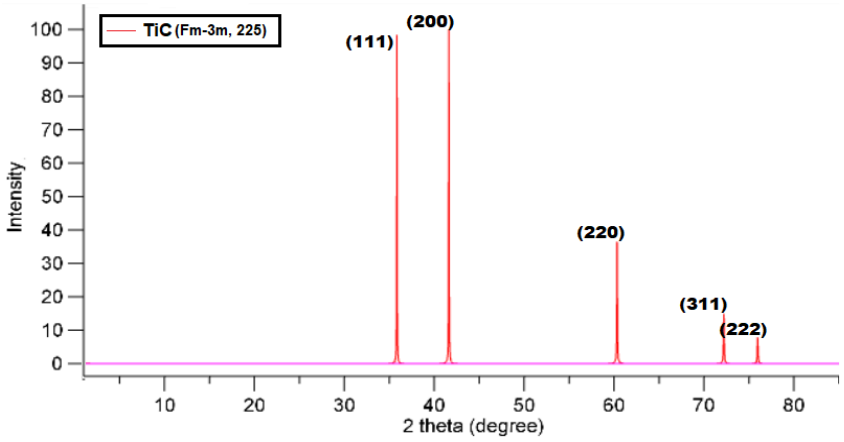

Figure 4: Simulated XRD spectrum of a cubic TiC crystal, generated with VESTA from ref. [51]. The spectrum shows five distinct peaks in the range of $0° < 2\theta < 80°$. From the VESTA calculation, peak positions and corresponding Miller planes can be identified.

material [50], which is on the order of Ångströms. In order for diffraction to occur, the x-ray wavelength that is used should be on the order of the lattice spacing ($\lambda \sim$ Å).

The atomic scattering cross section for x-rays used in XRD is low enough for the x-rays to penetrate into a solid up to a depth on the order of μm [44], allowing for contributions to the measured diffraction signal stemming from deep within a material. The (HfNbTaTiZr)C thin films produced by PLD have a thickness of 10-80nm. This means that the XRD signal of thin films in a regular XRD configuration would be dominated by the substrate. To avoid this, the samples are measured in a grazing incidence XRD (GIXRD) setup. In GIXRD, x-rays are incident under a fixed grazing angle w.r.t. the sample. The sample is kept fixed and the detector is rotated to measure intensity as a function of diffraction angle. Alternatively a 2-dimensional detection screen can be used to avoid rotation of the detector. GIXRD provides a method to measure structural properties of the thin film surface because of the increased optical path length caused by the grazing angle of the incident light.

3.3.2 Measurement Principle

In XRD, the spatial dependence of the intensity of diffracted x-ray photons is measured. In case of a perfect crystalline lattice, constructive interference will occur at incident angles that are a multiple of the x-ray wavelength ($n\lambda$; $n = 1, 2, ...$), according to the Bragg equation [50]:

$$n\lambda = 2d\sin(\theta), \tag{25}$$

where d is the distance between two individual lattice planes, λ is the wavelength of the x-rays, and θ is the angle of incidence.

An ideal crystal lattice has periodicity in three spatial dimensions. For simplicity one can view the a crystal structure as consisting of many layers of atomic planes of a crystal, oriented in the same direction. As a function of the incident angle, x-rays will encounter a different path length before encountering the next lattice plane. This path length difference introduces a phase difference between the incoming and outgoing x-rays. In case of out-of-phase reflections, no reflected signal is

recorded at the detector. For certain incident angles, in-phase reflections will cause a constructive interference in the reflected signal.

Because the spacing of the lattice planes of a crystal depends on the crystallographic direction w.r.t. a fixed point or plane in space, such as a crystal surface, it is convenient to recast the Bragg equation in terms of a systems Miller indices[2]:

$$n\lambda = 2d_{hkl}\sin(\theta_{hkl}), \tag{26}$$

with d_{hkl} corresponding to the lattice spacing of the crystal plane with Miller index (hkl), and θ_{hkl} the diffraction angle resulting from reflection off the crystal planes with Miller index (hkl). Figure 4 shows a simulated x-ray powder diffraction spectrum of cubic TiC (Fm-3m, 225), which contains multiple peaks corresponding to different Miller planes of the crystal structure.

In case of a single, polycrystalline material, a grain structure is present, with individual grains consisting of material along the same crystallographic directions. In between grains, there may be a global difference in crystallographic orientation w.r.t. a fixed angle of incidence of the x-rays. This can be caused by a rotation ϕ of a grain w.r.t. another grain. However, the conditions for constructive and destructive interference are set by the lattice spacing d_{hkl} and are therefore the same for all polycrystalline grains of the same material. The relative angle ϕ that may be present between grains causes the diffraction intensity to appear in a different location in three-dimensional space, which may be recorded either by a co-rotating detector arm or using a 2d- detector plate. To account for the spatial diffraction pattern an integrated intensity should be used.

Another possibility for a material is to solidify in an amorphous structure. The periodicity of a crystal lattice can be viewed as having a characteristic distance between atoms in three spatial directions on both the smallest (short-range order) and larger scales (long-range order). Amorphous systems do not have long-range order, and atoms in an amorphous system thus only have a local characteristic distance. The presence of short-range order causes some ordered structures to be present, off which x-rays can diffract locally. However, the condition of constructive and destructive interference is affected predominantly by the presence of long-range order, which is not present in amorphous materials. This causes broad regions of slightly increased intensity in case of XRD on amorphous samples, as opposed to narrow diffraction peaks observed in XRD on single- and polycrystalline samples [50].

3.3.3 Scherrer analysis of grain size broadening

In XRD spectra of real materials the diffraction peaks are not infinitely narrow. Examples of factors that broaden real XRD peaks are instrumental, strain, grain size, and thermal broadening. With appropriate consideration, XRD peak analysis can indicate difference in grain size. In room-temperature XRD measurements of small grains, thermal broadening can be ignored. Instrumental broadening is constant for the same setup. Furthermore strain contributions are assumed to be absent. Under these assumptions, any difference in observed full width at half maximum (FWHM) is assumed to be caused by grain size difference.

The relation between peak full width at half maximum (FWHM) and particle size in XRD is described by the Scherrer equation [50]:

$$L = \frac{K\lambda}{\beta_p(2\theta)\cos(\theta)}, \tag{27}$$

[2]Within a 3d crystal multiple planes exist along which the system is periodic. The system of Miller indices allows for describing all possible lattice planes and their symmetric equivalents for a given crystal space group.

where L is the average grain size (nm). $K = 0.94$ is a dimensionless shape factor [50], λ is the wavelength of the x-rays (nm), β_p is the contribution of particle size broadening effects to the FWHM of the observed FWHM β_{obs}, and 2θ is the diffraction angle of the peak. The wavelength that is used in the GIXRD setup is Cu K_α ($\lambda = 1.5406$ Å). The value of the shape factor $K = 0.94$ originates from the assumption that the crystallites that make up the individual grains are cubic [50].

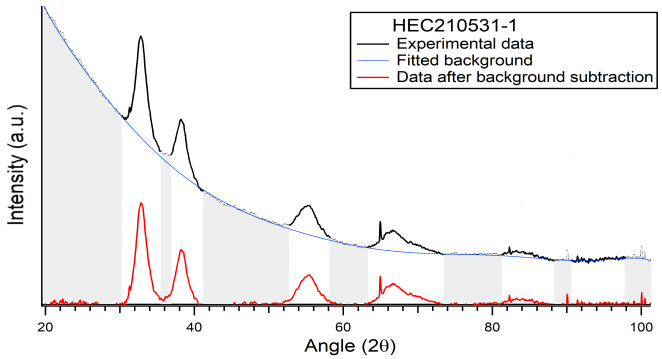

Figure 5: Background subtraction of XRD data (black line). The background of the experimental data is masked (grey area) and a polynomial of degree 10 is fit to the masked points (blue line). The background is subtracted from the experimental data, resulting in the background-subtracted XRD signal (red line).

The parameters β_{obs} and 2θ are extracted from fitting XRD spectra. To improve the fit accuracy a background subtraction was performed. Figure 5 shows an example of the background subtraction procedure, where a polynomial of degree 10 was fitted to the background signal.

It is possible to obtain an estimate for the particle size L by assuming that no strain or thermal broadening are present. It can furthermore be assumed that the particle size broadening and instrumental broadening are well-described by a Gaussian FWHM. If this assumption is made, the Gaussian components of β_{obs} can be separated as [50]:

$$\beta_{obs}^2 = \beta_p^2 + \beta_{setup}^2 \rightarrow \beta_p = \sqrt{\beta_{obs}^2 - \beta_{setup}^2}, \tag{28}$$

which allows for rewriting of equation 27 in terms of the observed broadening β_{obs} and β_{setup} as:

$$L = \frac{K\lambda}{\beta_p(2\theta)\cos(\theta)} = \frac{K\lambda}{\cos(\theta)\sqrt{\beta_{obs}(2\theta)^2 - \beta_{setup}^2}} \tag{29}$$

where L is the average size of the particles in nm under the assumption that the only contributions to the observed FWHM are from particle broadening and instrumental broadening. The data is fitted with a Gaussian function with a prefactor $A = \frac{1}{\sigma\sqrt{2\pi}}$ and width $W = \sigma\sqrt{2}$:

$$f(x) = y_0 + A\exp(-\Big(\frac{(x - x_0)}{W}\Big)^2), \tag{30}$$

for which the FWHM β is given by:

$$\beta = 2\sigma\sqrt{2\ln(2)} = W\sqrt{2}\sqrt{2\ln(2)}. \tag{31}$$

4 Results

The effects of laser fluence on surface composition were investigated through a series of depositions on Si(100) performed in UHV. The results are introduced in section 4.1. The effects of Ar and Ne pressures on surface composition were evaluated for a fixed laser fluence. Sections 4.2.1, 4.2.2 introduce the results of surface composition as a function of Ar, Ne pressure, respectively. The optimization procedure has led to near-equiatomic surface composition of metals and carbon in (HfNbTaTiZr)C, which is further discussed in section 4.4. Section 4.3 discusses reproducibility between depositions and section 4.5 discusses thickness calibration of the deposited films.

To confirm that PLD can synthesize rock salt (HfNbTaTiZr)C thin films, samples were measured with XRD. Section 4.6 discusses peak position, peak width and grain size derived from XRD spectra of (HfNbTaTiZr)C deposited on Si(100) and $Al_2O_3(0001)$. Lastly a difference between (HfNbTaTiZr)C on Si(100) and $Al_2O_3(0001)$ is reported in section 4.7.

4.1 PLD process parameters and stoichiometry

4.1.1 Effect of deposition fluence on film composition in ultra-high vacuum

A series of test depositions were performed in UHV ($p_{T,\mathrm{UHV}} < 4 * 10^{-8}$ mbar). The metal and carbon content was determined with XPS by analysing the peak area of Hf $4d$, Ta $4d$, Nb, Zr $3d$, Ti $2p$ and C $1s$ transitions. Figure 6 shows an example of the fits that have been used to extract peak area of the relevant transitions.

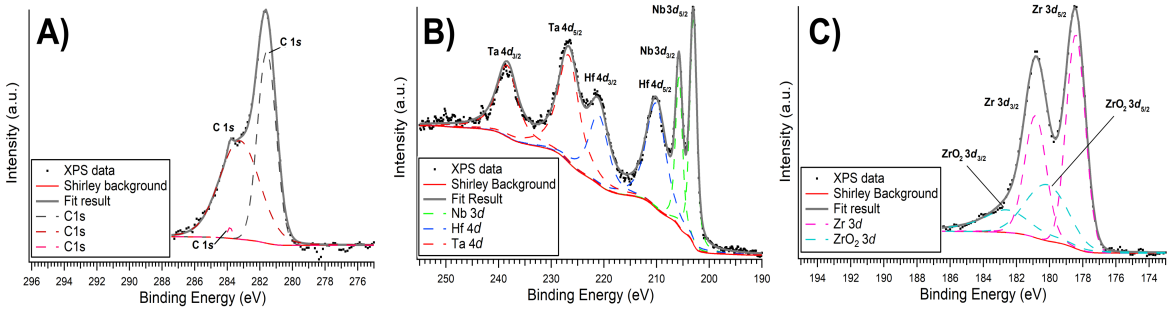

Figure 6: Experimental data, Shirley background and individual fitted peak used to determine the total area of A) C $1s$ region, B) Ta $4d$, Hf $4d$ and Nb $3d$ region, and C) Zr $3d$ region. For the C $1s$ region in A) multiple peaks were used to determine the total area. The fits in region A) were not used for chemical interpretation. For the Zr $3d$ region in figure C an additional peak was required to accurately determine the total area.

First, a series of depositions were performed at fluences of 6-8 J/cm^2 and a repetition rate of 3Hz. Secondly, a series of depositions were performed at fluences of 7-14 J/cm^2 and a repetition rate of 10Hz. Figure 7 shows the composition of the samples deposited in UHV at 6-8 J/cm^2 (fig. 7A, B) and 7-14 J/cm^2 (fig. 7C, D). Figures 7A and 7C show the relative concentration of metals w.r.t. the total amount of metals in the sample, n_M, which is defined as the area of metal i, M_i, normalized to the total sum of metal $M_T = \sum M_j$. Figures 7B and 7D show the relative concentration of carbon to the sum of metal and carbon, n_C, which is defined as the total amount of carbon C normalized to the sum of carbon and total metals $C + \sum M_j$.

Figure 7A shows a trend of increasing Ta and decreasing Nb concentration as a function of increasing deposition fluence. The increase of Ta concentration at higher deposition fluences is

attributed to the high melting point of TaC [37]. The decrease of NbC between a deposition fluence of 7 to 8 J/cm^2 may be caused by a higher concentration of Ta in this range of fluence and a subsequent increased rate of resputtering at the substrate. The results of Ti concentration are not congruent with this explanation, since resputtering is thought to affect mainly the lightest elements at the substrate, and the Ti concentration is observed to increase between a deposition fluence of 7 and 8 J/cm^2.

Figure 7C shows a similar trend of increasing Ta concentration as well as an increasing Nb concentration at higher deposition fluence. Furthermore figure 7C shows a decrease in Ti concentration at higher deposition fluences. The decrease of Ti concentration supports the explanation of increased resputtering of Ti by Ta, caused by a higher concentration of Ta in case of higher deposition fluence. The largest difference in Ti concentration is observed between a fluence of 7 and 10 J/cm^2, where an increase of Ta concentration is apparent.

The ratio of carbon to the sum of carbon and metals in figure 7B shows an average carbon-to-total metal concentration of 65% for deposition fluences in the range 6-8 J/cm^2, an excess of 15% w.r.t. an equiatomic carbon-to-total metal ratio of 50%. Figure 7D shows an average carbon content of 67% for a deposition fluence in the range of 7-14 J/cm^2, which indicates a carbon excess of 17%, similar to the results for 6-8 J/cm^2. It is thought that the carbon excess is caused by a lack of stoichiometric transfer of metals for PLD of (HfNbTaTiZr)C, predominantly caused by melt ejection and resputtering. These results suggest that a process gas may circumvent this problem by suppressing carbon concentration.

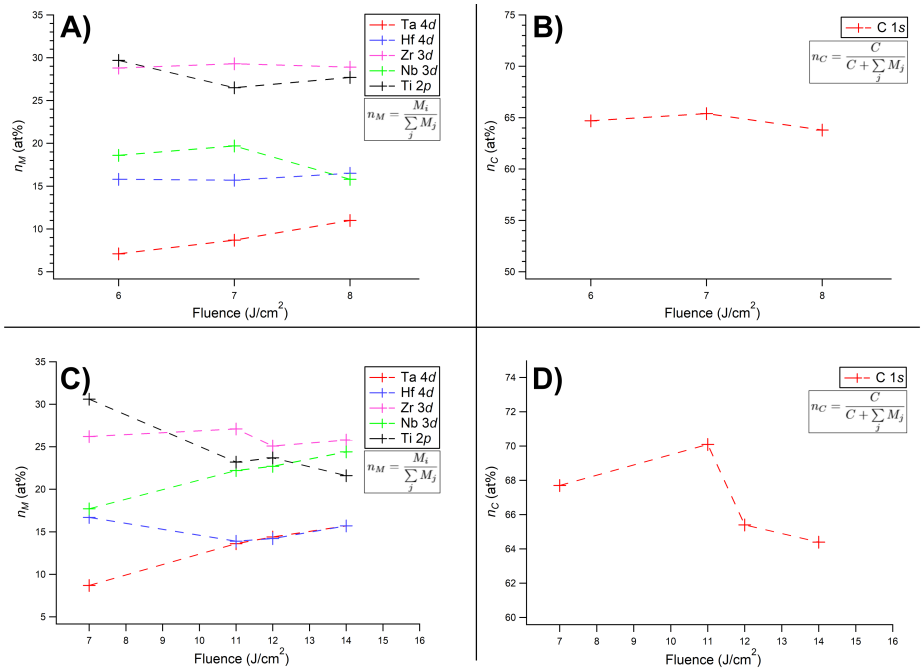

Figure 7: Metal-to-metal concentration n_M and carbon-to-total metal concentration n_C of (HfNbTaTiZr)C thin films deposited in UHV. The results in figures A) and B) are from samples deposited at 3Hz, 6-8 J/cm^2. The results in figures C) and D) are from samples deposited at 10Hz, 7-14 J/cm^2. The y-axes in figures A) and C) plot metal-to-metal concentration n_M. The y-axes in figures B) and D) plot carbon-to-total metal concentration n_C.

4.2 Effect of process gas pressure on film composition

4.2.1 Composition of Argon-deposited films

The presence of a process gas is thought to affect the scattering of plasma constituents, and thereby affect the film composition. Figure 8 shows n_M and n_C of (HfNbTaTiZr)C films deposited in Ar at a deposition pressure of $8*10^{-2}$ mbar and $2*10^{-1}$ mbar. The deposition pressure in figure 8 is the total pressure in case of the presence of a process gas.

The pressure dependence of surface composition in Ar gas is not the same as the fluence dependence in UHV that was discussed in the previous section. Together, F and p form a 3D parameter space that describes the surface composition. In figure 7, p was kept fixed and F is varied, whereas in figure 8, F was kept fixed and p is varied. The results on surface composition as a function of process gas pressure (Ar and Ne) can be thought of as lying in a plane along the z-axis that intersects figure 7 at a fixed fluence. The z-axis represents the total pressure p_T and the results on surface composition in UHV are at a process gas pressure equal to 0.

Figure 8A shows a trend of strongly increasing Ta and strongly decreasing Ti concentration as a function of increasing deposition pressure. Most importantly the figure shows a crossover point of Ta and Ti concentration in between a deposition fluence of $8*10^{-2}$ mbar and $2*10^{-1}$ mbar. Furthermore figure 8 shows a trend of slightly increasing Hf concentration as a function of increasing deposition pressure. The samples deposited in Ar exhibit an imbalance of the content of heavy and light metals. It is thought that the Ta increase and Ti decrease both originate in scattering effects. Ti is the lightest metal in the deposition plasma, whereas Ta is the heaviest metal. The significantly lighter Ti is scattered at larger angles, increasing the probability for a Ti atom in the deposition plasma to miss the deposition substrate. Because the mass of Hf is comparable to Ta, it shows a slight increase as function of pressure. Zr and Nb are lighter than Ta, but significantly heavier than Ti, and therefore show a smaller decrease in concentration at higher deposition pressures.

Figure 8B shows a trend of increasing n_C as a function of increasing deposition pressure. The average value of n_C for samples deposited in Ar is 56.5%. Compared to the average concentration of carbon in figure 7, the presence of Ar gas reduces n_C by 10% on average, resulting in an average carbon excess of 6.5% w.r.t. an equiatomic metal-to-carbon ratio. The suppression of carbon excess through presence of a process gas was anticipated. However a higher carbon concentration at a deposition pressure of $2*10^{-1}$ mbar was not expected. Through the scattering argument, the carbon concentration is expected to decrease at higher deposition pressures, and therefore no conclusive explanation is given for this effect.

Combining the results in figures 7 and 8 implies that samples deposited in Ar are closer to near-equiatomic composition in both metal and carbon concentration as compared to samples deposited in UHV. The large decrease in Ti concentration at higher deposition pressure is thought to originate a combination of preferential scattering of Ti atoms by Ar due to the lower mass of Ti compared to the other metals in the deposition plasma and increased resputtering of Ti by Ta at the deposition substrate.

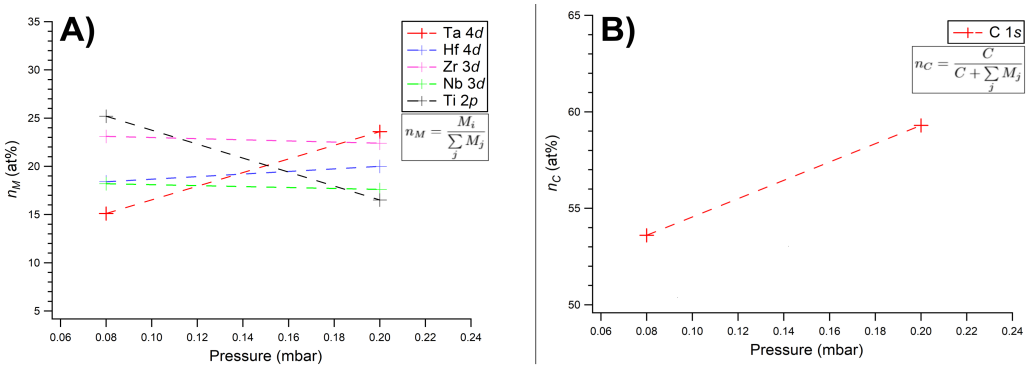

Figure 8: Metal-to-metal concentration n_M and carbon-to-total metal concentration n_C of (HfNbTaTiZr)C thin films deposited in Ar. Figure A) shows the concentration of individual metals w.r.t. the total amount of metal in the films, n_M. Figure B) shows the carbon content w.r.t. the total amount of metal and carbon in the films, n_C.

4.2.2 Composition of Neon-deposited films

As aforementioned, it is thought that Ti is scattered preferentially by Ar gas atoms due to its low mass compared to the other metals in the deposition plasma. By reducing the mass of the process gas the effect of Ti deficiency is expected to be suppressed. A series of depositions with varying deposition pressure in Ne were performed at two fixed deposition fluences. Figure 9 shows the pressure dependence of the composition of samples deposited at a fluence of 10 J/cm^2 (fig. 9A, B) and 12 J/cm^2 (fig. 9C, D). Figures 9A and 9C show the relative concentration of metals n_M. Figures 9B and 9D show the carbon-to-total metal concentration n_C. The deposition pressure in figure 9 is the total pressure in case of the presence of a process gas.

Figure 9A shows an increase of Ta and Hf concentration, and a decrease in Ti, Zr and Nb concentration between deposition pressures of 8*10^{-2} mbar and 4*10^{-2} mbar. The increase of Ta and Hf and decrease of lighter Nb, Zr and Ti are congruent with the explanation of preferential scattering of lighter masses at higher deposition pressure. In case of Ne depositions the decrease of Ti concentration is lower as compared to the decrease in Zr or Nb. Both effects are more strongly visible in figure 9B. The results in 9B were obtained at a deposition fluence of 12 J/cm^2, causing a high concentration of metals that originate from metal carbides with high melting temperature (TaC, HfC). In between deposition fluence of 10 and 12 J/cm^2 the average Ti, Zr, Nb concentration was lowered relative to Ta and Hf. It is thought that the preferential scattering of lighter masses causes an even higher concentration of Ta and Hf at the deposition substrate, which strengthens resputtering of Nb, Zr and Ti by the heavier metals Ta and Hf.

In figure 9B and 9D, it can be seen that the average carbon content is close to 50%, 40% for deposition at 10, 12 J/cm^2, respectively. The carbon-to-total metal ratio shows an increase at higher deposition pressure at a deposition fluence of 10 J/cm^2 as opposed to a decrease at a deposition fluence of 12 J/cm^2. The decrease of carbon concentration at higher deposition fluence is attributed to the increased concentration of Hf and Ta at a deposition fluence of 12 J/cm^2.

The results in figure 9 show a lower carbon excess for depositions in Ne as compared to depositions in Ar for deposition fluences of 10 and 12 J/cm^2. This result can not be explained solely through mass-dependent scattering, from which a higher carbon excess in Ne would be expected.

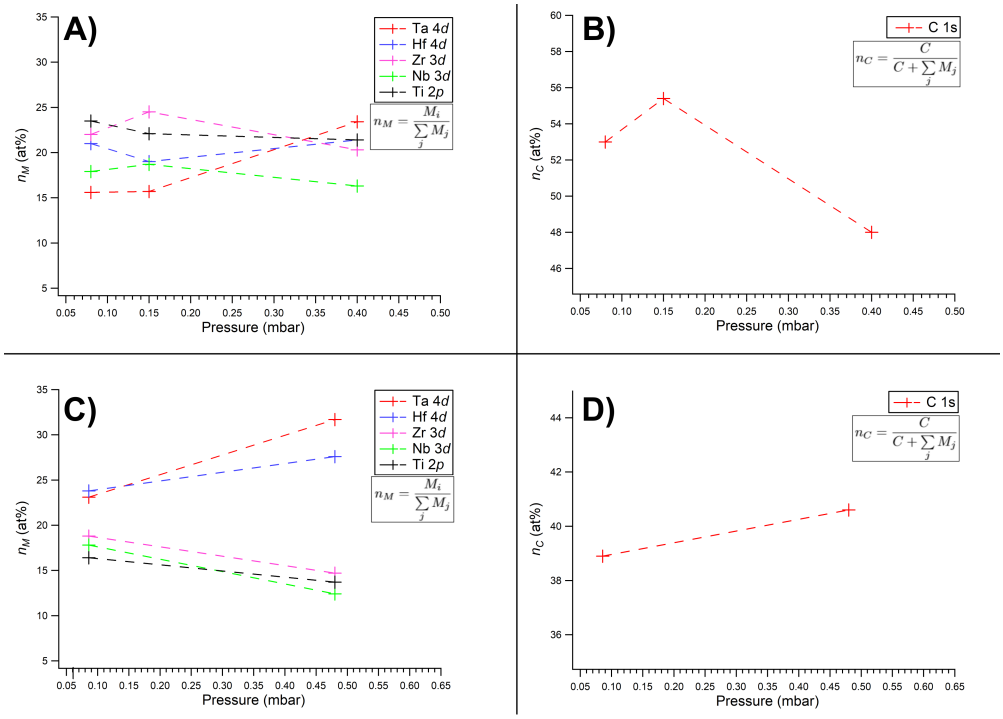

Figure 9: Composition of metal and carbon of (HfNbTaTiZr)C thin films deposited in Ne. Figures A) and C) shows the concentration of individual metals w.r.t. the total amount of metal in the films at a fluence of 10, 12 J/cm^2, respectively. Figures B) and D) show the carbon content w.r.t. the total amount of metal and carbon in the films at a fluence of 10, 12 J/cm^2, respectively.

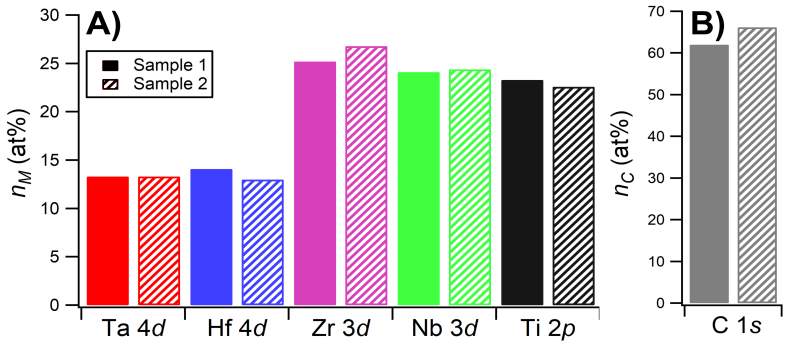

Figure 10: Metal and carbon composition of two samples deposited 1hr apart. Figure A) shows the relative concentration of individual metals to the total amount of metals. Figure B) shows the concentration of carbon relative to the total amount of carbon and metal in the films.

4.3 Reproducibility in PLD of (HfNbTaTiZr)C

Reproducibility has been tested in UHV between depositions by analysing the metal and carbon content between two depositions performed 1hr apart. All process parameters were kept fixed and the only potential cause of variations was the introduction of a new deposition substrate into the PLD chamber. Figure 10A shows that the metal-to-metal concentrations between depositions lies within a range of 1-2 %. Figure 10B shows that the carbon-to-total metal ratio lies in a larger range close to 4%. It is thought that the carbon content of (HfNbTaTiZr)C thin films deposited with PLD depends on the cleanliness conditions of the UHV chamber, PLD target surface and deposition substrate. A potential cause of the discrepancy in carbon concentration is that the carbon concentration on the PLD target surface may differ from the carbon concentration slightly below the PLD target surface, and that this difference in concentration may be exposed after pre-ablation and deposition. Another possible explanation for the discrepancy in carbon concentration is the introduction of a new deposition substrate into the PLD chamber, which may introduce different cleanliness conditions and initial chamber pressure.

4.4 Near-equiatomic PLD of (HfNbTaTiZr)C on Si(100) in Ne

Near-equiatomic composition of metals and carbon was achieved for the optimized recipe in Ne. Figure 9A shows that at 10 J/cm^2, and 10Hz, the optimal composition lies within a range of 15-25 at%. It should be noted that the concentration of Ta and Nb appears to be substoichiometric in case of lower deposition pressures. Nb concentration appears to be substoichiometric for all deposition pressures that were considered at 10 J/cm^2. It can furthermore seen from figure 9B that the average carbon-to-total metal concentration is close to 50 %. An optimal concentration of metals and carbon is expected at a deposition pressure of 3*10^{-2} mbar, with the only caveat that Nb is expected to be substoichiometric.

Figure 9C shows that the metal-to-metal ratio of samples deposited at 8*10$^-$2 mbar, 12 J/cm^2 and 10Hz is within the range of 15-25 at%. The results indicate that the control of PLD process parameters allowed for near-equiatomic metal composition of all five metals in a range of 15-25 at% and a carbon-to-total metal ratio close to 50%.

The findings on reproducibility should be considered for the validity of the result on near-equiatomic (HfNbTaTiZr)C. The observed variation of metal concentration of 1-2 % implies that the results on metallic concentration in near-equiatomic (HfNbTaTiZr)C falls well within the empirical rule of 5-35% for high entropy alloys. The observed variation in carbon concentration implies that the carbon-to-total metal ratio observed in the near-equiatomic deposition of (HfNbTaTiZr)C is close to the desired value of 50%.

4.5 Thickness calibration of PLD-synthesized (HfNbTaTiZr)C thin films

An optimized recipe in Ne was deposited onto a Si(100) substrate covered in two locations with a droplet of photoresistive material in order to create a sharp step. The photoresist was washed off with acetone after deposition exposing the Si(100) substrate. From 5 profilometry measurements a height difference between Si substrate and (HfNbTaTiZr)C thin film was measured of 48nm ± 3nm. The uncertainty is the standard deviation of five profilometry measurements. It should be noted that the deposition rate is dependent on the incoming flux of plasma constituents, which in turn depends on the background pressure as well as the process gas. The calibration was performed at a Ne pressure of 10^{-2} mbar and deposition fluence of 10 J/cm^2, for 9000 shots.

4.6 XRD analysis of PLD-synthesised (HfNbTaTiZr)C thin films

4.6.1 Rock salt formation of (HfNbTaTiZr)C on Si(100) and Al_2O_3(0001)

To verify the formation of rock salt (HfNbTaTiZr)C XRD analysis was performed on samples deposited on Si(100) and Al_2O_3(0001). The peak position 2θ and FWHM β_{obs} were extracted from a Gaussian fit to the intensity as a function of diffraction angle. Figure 11 shows the XRD spectra of (HfNbTaTiZr)C deposited on Si(100) and Al_2O_3(0001). The fit parameters are summarized in table 4. The fit uncertainty and Gaussian width uncertainty that are reported are assumed to be below the experimental error present in the XRD setup.

The results in table 4 can be compared with the diffraction angles of x-ray powder diffraction spectra of cubic binary carbides NbC [52], ZrC [53], HfC [54], TaC [55] and TiC [51] generated in VESTA, which are listed in table 5. The diffraction angles of (HfNbTaTiZr)C on Si(100) and Al_2O_3(0001) fall within the range expected from cubic binary carbides: RS(111), RS(200), RS(220) and RS(311). These results indicate a polycrystalline structure of (HfNbTaTiZr)C on Si(100) and Al_2O_3(0001).

The diffraction peaks of (HfNbTaTiZr)C on both substrates show a different peak width, which is assumed to be caused by a grain size difference between deposition substrates.

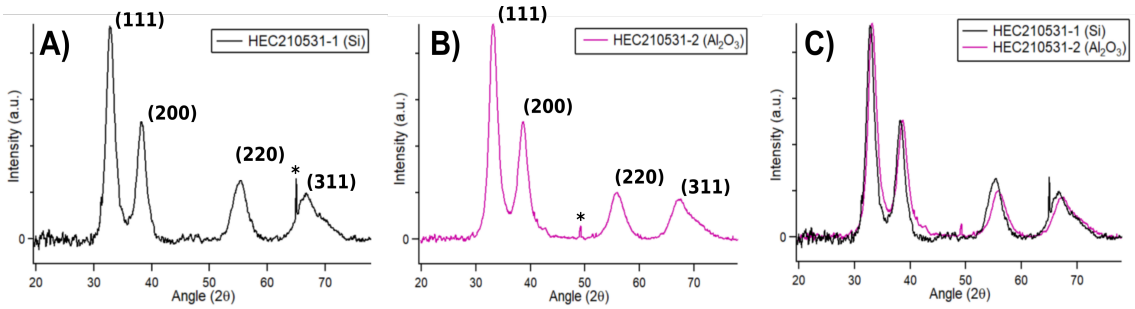

Figure 11: XRD spectra of (HfNbTaTiZr)C deposited on A) Si(100) and B) Al_2O_3(0001). Figure C) shows a comparison between the two XRD spectra. The corresponding peaks have been annotated with Miller indices (*hkl*). Peaks that stem from detector noise are indicated with an asterisk (*).

Substrate	**Diffraction peak**	2θ (°)	W_{obs} (°)	L (nm)
Si(100)	HEC(111) (RS)	32.89 ± 0.01	1.02 ± 0.01	5.3
	HEC(200) (RS)	38.26 ± 0.01	1.14 ± 0.02	
	HEC(220) (RS)	55.26 ± 0.01	1.75 ± 0.02	
	HEC(311) (RS)	67.07 ± 0.04	2.92 ± 0.08	
Al_2O_3(0001)	HEC(111) (RS)	33.26 ± 0.01	1.11 ± 0.02	4.9
	HEC(200) (RS)	38.64 ± 0.01	1.18 ± 0.02	
	HEC(220) (RS)	55.94 ± 0.01	1.85 ± 0.02	
	HEC(311) (RS)	67.87 ± 0.03	3.03 ± 0.05	

Table 4: Results of XRD peak analysis of (HfNbTaTiZr)C deposited on Si(100) and Al_2O_3(0001). The table shows diffraction angles 2θ and observed width of Gaussian fits W_{obs} for (HfNbTaTiZr)C deposited on Si(100) and Al_2O_3(0001). The grain size estimate L for (HfNbTaTiZr)C deposited on Si(100) and Al_2O_3(0001) was determined from the HEC(111) diffraction peak for Si(100) and Al_2O_3(0001). The estimation includes the subtraction of instrumental broadening.

2θ (°)	NbC	ZrC	HfC	TaC	TiC
RS (111)	31.86	32.81	33.38	34.64	35.84
RS (200)	36.95	38.06	38.69	40.20	41.62
RS (220)	53.26	54.92	55.86	58.17	60.33
RS (311)	63.41	65.47	66.63	69.50	72.20

Table 5: Simulated x-ray powder diffraction angles of binary carbides. The peak position of the (111), (200), (220) and (311) planes were simulated with VESTA [52, 53, 54, 55, 51].

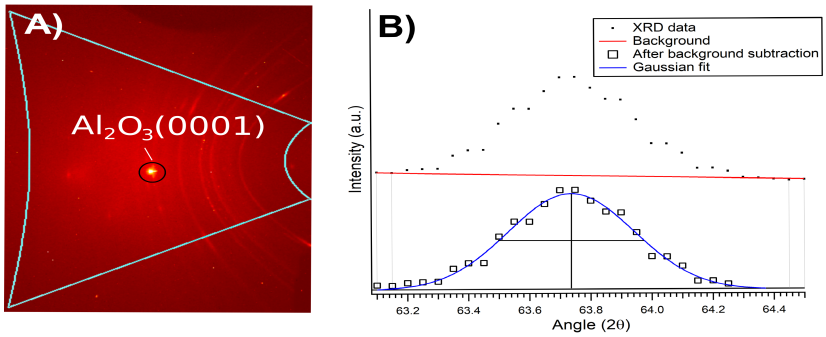

Figure 12: XRD spectrum of an $Al_2O_3(0001)$ single crystal substrate which was used to determine instrumental broadening. Figure A) shows the 2D-detector image dominated by a a high-intensity spot stemming from the $Al_2O_3(0001)$ substrate. Figure B) shows an integrated intensity of the measured sample in red, and a Gaussian fit to the peak after background subtraction in blue.

4.6.2 Grain size estimate of (HfNbTaTiZr)C on Si(100) and $Al_2O_3(0001)$

The difference in FWHM between (HfNbTaTiZr)C on Si(100) and $Al_2O_3(0001)$ is visible in figure 11C where an overlay of the XRD spectra is shown. Furthermore table 4 shows a difference in W_{obs} between Si(100) and $Al_2O_3(0001)$. Under the assumption of particle size broadening an increased FWHM indicates a smaller grain size according to the Scherrer equation.

The instrumental broadening of the XRD setup is required for the estimation of average particle size L. Figure 12 shows the 2D-detector image and integrated intensity of the XRD measurement performed on a sample with an exposed $Al_2O_3(0001)$ substrate. It is assumed that no strain, temperature or particle size broadening effects are present in the XRD spectrum of the $Al_2O_3(0001)$ substrate, and that the instrumental broadening is Gaussian. From figure 12 it can be estimated that the FWHM of instrumental broadening $\beta_{setup} \approx 0.48° \approx 0.008$ rad. For the estimation of average grain size L the HEC(111) diffraction peak was used (table 4). The results indicate a relative difference in grain size between (HfNbTaTiZr)C deposited on Si(100) and $Al_2O_3(0001)$ of $\sim 8\%$. The accuracy of the estimation is thought to be low and the results should be treated as indicative. However the observed difference in FWHM between XRD spectra on Si(100) and $Al_2O_3(0001)$ is thought to be a real effect. Alternatively, under the aforementioned assumptions, the broadening of the XRD peaks may originate in stoichiometry distribution between grains, causing different diffraction conditions for indivudal grains. Another origin of the peak broadening could stem from a preferred crystallite shape which affects the shape factor K in the Scherrer equation.

4.7 Substrate differences between (HfNbTaTiZr)C on Si(100) and Al_2O_3(0001)

A sample batch was produced consisting of two Si(100) and two Al_2O_3(0001) substrates mounted on the same sample plate. In order to force oxidation to occur, the samples were exposed to ambient conditions. After a period of 2 weeks two of the samples were analysed with XPS.

A difference in visual appearance and carbon content was observed for samples deposited on Si(100) and Al_2O_3(0001). Figure 13 shows the difference in visual appearance between (HfNbTaTiZr)C deposited on Al_2O_3(0001) and Si(100). Figure 14A, B shows the XPS spectrum of the C 1s region for (HfNbTaTiZr)C deposited on Si(100), Al_2O_3(0001), respectively, after ambient oxidation. Both XPS measurements were performed on region a) from figure 13. The results in figure 14 indicate a difference in intensity ratio between the peak close to 282 eV and the peak close to 284.5 eV. Considering the binding energies of metal carbides [46, 56] it was assumed that the peaks around 282 eV in figure 14A, B stem from metal carbide bonds. The origin of the peak around 285 eV in figure 14A, B are assumed to from carbon-carbon bonds.

The area of the peaks stemming from metal carbides was compared against the total peak area of carbon. The sum of the area of MC and non-MC peaks was used to normalize the ratio $n_{MC} = {}^{MC}/_{\sum C}$. The area ratio of peaks stemming from metal carbides to the area of peaks stemming from other carbon species was calculated to be 36%, 34% for Al_2O_3(0001), Si(100), respectively.

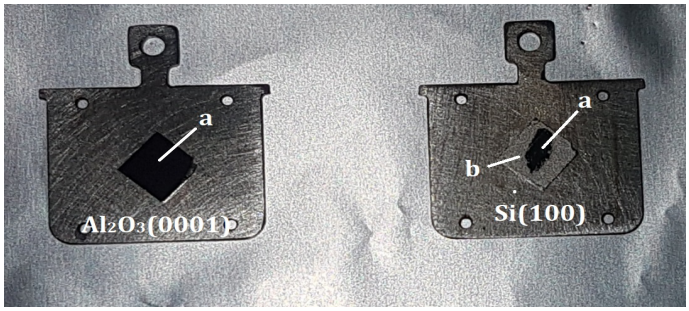

Figure 13: Visual appearance of (HfNbTaTiZr)C deposited on Al_2O_3(0001) (left) and Si(100) (right). The deposition on Al_2O_3(0001) shows a single, smooth and reflective region (a). The deposition on Si(100) shows a similar reflective region in the center of the film and a region (b) exclusive to Si(100), which is non-reflective and rough in visual appearance.

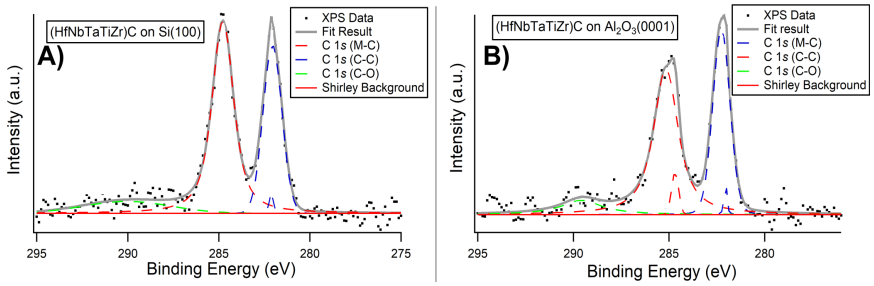

Figure 14: Qualitative differences between XPS spectra of (HfNbTaTiZr)C thin films deposited on Si(100) and Al_2O_3(0001). Figure A shows the C 1s spectrum of PLD-synthesized (HfNbTaTiZr)C on Si(100). Figure B) shows the C 1s spectrum of PLD-synthesized (HfNbTaTiZr)C on Al_2O_3(0001).

5 Conclusion & Outlook

PLD of a HfC:NbC:TaC:TiC:ZrC stoichiometric target resulted in (HfNbTaTiZr)C thin films grown on Si(100) and Al_2O_3(0001). The surface composition of resulting thin films was analysed with XPS and crystal structure was determined with XRD. Initial results on the fluence dependence of the surface composition of (HfNbTaTiZr)C thin films deposited in UHV indicated a lack of stoichiometric transfer of metals and an excess of carbon stoichiometry in PLD of multi-elemental metal carbide targets. The origin of off-stoichiometric transfer was discussed in context of ablation of multi-elemental targets, melt ejection, scattering of plasma and process gas, and resputtering at the deposition substrate. The surface composition was optimized towards near-equiatomicity by varying PLD process parameters. A (HfNbTaTiZr)C thin film with near-equiatomic composition was deposited on Si(100). XRD analysis confirmed polycrystalline rock salt (HfNbTaTiZr)C on both Si(100) and Al_2O_3(0001) substrates. An average grain size was estimated from the FWHM obtained from fitting after subtraction of instrumental broadening.

In conclusion, it is shown that the ability of controlling surface composition in PLD through available process parameters has resulted in near-equiatomic (HfNbTaTiZr)C thin films. The observed carbon-to-total metal ratio close to 1:1 supports the formation of a rock-salt metal carbide structure. Ultimately, the XRD results support the presence of a high entropy rock salt phase and the results on metallic surface composition of (HfNbTaTiZr)C fall well within the empirical 5-35% definition of high entropy materials, showing the potential of PLD for synthesis of high entropy materials, potentially for a wider range of target compositions. An outlook on future experiments follows below.

From literature on solid solution (HfNbTaTiZr)C an enhanced hardness is expected as compared to binary refractory metal carbides [9, 11]. Nanoindentation is a suitable technique for measuring hardness of thin films and could thereby confirm if an enhanced hardness is present in (HfNbTaTiZr)C thin films as compared to PLD-synthesized binary refractory metal carbides. A confirmation of enhanced hardness with nanoindentation experiments could further support the presence of a high entropy phase in PLD-synthesized (HfNbTaTiZr)C. Initial nanoindentation measurements have been performed, but have not yielded conclusive results due to experimental difficulties with a recently installed setup.

For future experiments on related high entropy materials, atomic force microscopy measurements can provide a reference value of grain size to compare to the values obtained from XRD analysis. Atomic force microscopy on (HfNbTaTiZr)C can furthermore characterize surface topography, which in combination with hardness measurements can be of interest for friction studies due to the reported low wear rate and friction coefficient of polycrystalline (HfNbTaTiZr)C [12].

References

[1] Cantor B., Chang I. T. H., Knight P., and Vincent A. J. B. Microstructural development in equiatomic multicomponent alloys. *Mater. Sci. Eng. A*, 375-377:213–218, 2004.

[2] Yeh J-W., Chen S-K., Lin S-J., Gan J-Y., Chin T-S., Shun T-T., Tsau C-H., and Chang S-Y. Nanostructured High-Entropy Alloys with Multiple Principal Elements: Novel Alloy Design Concepts and Outcomes. *Adv. Eng. Mater.*, 6(5):299–303, 2004.

[3] George E. P., Raabe D., and Ritchie R. O. High-entropy alloys. *Nat. Rev. Mater.*, 4:515–534, 2019.

[4] Zhang R. and Reece M. J. Review of High Entropy Ceramics: design, synthesis, structure and properties. *J. Mater. Chem. A*, 39(7):22148–22162, 2019.

[5] Oses C., Toher C., and Curtarolo S. High-entropy ceramics. *Nat. Rev. Mater.*, 5:295–309, 2020.

[6] Antusch S., Reiser J., Hoffman J., and Onea A. Refractory Materials for Energy Applications. *Energy Technol.*, 5:1064–1070, 2017.

[7] Yan X., Constantin L., Lu Y., Silvain J., Nastasi M., and Cui B. $(Hf_{0.2}Zr_{0.2}Ta_{0.2}Nb_{0.2}Ti_{0.2})C$ high-entropy ceramics with low thermal conductivity. *J. Am. Ceram. Soc.*, 101:4486–4491, 2018.

[8] Chen H., Xiang H., Dai F., Liu J., Lei Y., Zhang J., and Zhou Y. High porosity and low thermal conductivity high entropy $(Zr_0.2Hf_0.2Ti_0.2Nb_0.2Ta)C$. *J. Mater. Sci. Tech.*, 35:1700–1705, 2019.

[9] Sarker P., Harrington T., Toher C., Oses C., Samiee M., Maria J-P., Brenner D. W., Vecchio K. S., and Curtarolo S. High-entropy high-hardness metal carbides discovered by entropy descriptors. *Nat. Comm.*, 9:4890.1–4890.10, 2018.

[10] Harrington T. J. et al. Phase stability and mechanical properties of novel high-entropy transition metal carbides. *Act. Mater.*, 166:271–280, 2019.

[11] Wang Y., Csanádi T., Zhang H., Dusza J., Reece M. J., and Zhang R-Z. Enhanced Hardness in High-Entropy Carbides through Atomic Randomness. *Adv. Theory. Simul.*, 3(2000111):1–8, 2020.

[12] Braic V., Vladescu A., Balaceanu M., Luculescu C., and Braic M. Nanostructured multi-element (TiZrNbHfTa)N and (TiZrNbHfTa)C hard coatings. *Surf. Coat.*, 211:117–121, 2012.

[13] Braic V., Balaceanu M., Braic M., Vladescu A., Panseri S., and Russo A. Characterization of multi-principal-element (TiZrNbHfTa)N and (TiZrNbHfTa)C coatings for biomedical applications. *J. Mech. Behav. Biomed. Mater.*, 10:197–205, 2012.

[14] Sun Q., Tan H., Zhu S., Zhu Z., Wang L., Cheng J., and Yang J. Single phase (Hf-Mo-Nb-Ta-Ti)C high entropy ceramic: a potential high temperature anti-wear material. *Tribol. Int.*, 157(106883):1–9, 2021.

[15] Braic M. Vladescu A. Panseribc S. Braic V., Balaceanua M. and Russob A. Characterization of multi-principal-element (TiZrNbHfTa)N and (TiZrNbHfTa)C coatings for biomedical applications. *J. Mech. Behav. Biomed. Mater.*, 10:197–205, 2012.

[16] Dekhtyar Y. Jinga V. Pruna V. Balaceanu M. Dinu M. Pana I. Vendina V. Vladescu A., Titorencu I. and Braic M. *In Vitro* Biocompatibility of Si Alloyed Multi-Principal Element Carbide Coatings. *PLOS ONE*, 11(8):1–18, 2016.

[17] Zhang Q., Zhang J., Li N., and Chen W. Understanding the electronic structure, mechanical properties, and thermodynamic stability of (TiZrHfNbTa)C combined experiments and first-principles simulation. *J. Appl. Phys.*, 126(2):025101.1–025101.6, 2019.

[18] Zhou J., Zhang J., Zhang F., Niu B., Lei L., and Wang W. High entropy carbide: a novel class of multicomponent ceramics. *Ceram. Int.*, 44(17):22014–22018, 2018.

[19] Ye B., Wen T., Huang K., Wang C-Z., and Chu Y. First-principles study, fabrication, and characterisation of $(Hf_{0.2}Zr_{0.2}Ta_{0.2}Nb_{0.2}Ti_{0.2})C$ high-entropy ceramic. *J. Am. Ceram. Soc.*, 102:4344–4352, 2019.

[20] Feng L., Chen W., Fahrenholtz W., and Hilmas G. Strength of single-phase high-entropy carbide ceramics up to 2300 °C. *J. Am. Cer. Soc.*, 104(1):419–427, 2021.

[21] Rost C. M., Borman T., Hossain M. D., Lim M., Quiambo-Tomko K. F., Tomko J., Brenner D. W., Maria J-P., and Hopkins P. E. SUPPLEMENTAL MATERIAL: Carbon bonding controls the thermal conductivity mechanisms in high entropy carbide thin films. pages 1–10, 2020.

[22] Hossain M., Borman T., and Maria J-P. Bi-polar High-Power Impulse Magnetron Sputtering (HiPIMS) synthesis of high entropy carbides. *ResearchGate*, pages 1–16, 2021.

[23] Fähler S., Sturm K., and Krebs H.-U. Resputtering during the growth of pulsed-laser-deposited metallic films in vacuum and in ambient gas. *Appl. Phys. Lett.*, 75(24):3766–3768, 1999.

[24] Sturm K., Fähler S., and Krebs H.-U. Pulsed laser deposition of metals in low pressure inert gas. *Appl. Surf. Sci*, pages 462–466, 2000.

[25] Lutey A. H. A. An improved model for nanosecond pulsed laser ablation of metals. *J. Appl. Phys.*, 114(083108):1–10, 2013.

[26] Hossain M. D., Borman T., Kumar A., Chen X., Khosravani A., Kalidindi S. R., Paisley E. A., Esters M., Oses C., Toher C., Curtarolo S., LeBeau J. M., Brenner D., and Maria J-P. Carbon stoichiometry and mechanical properties of high entropy carbides. *Act. Mater.*, 215(15):1–10, 2021.

[27] Dunhalde S., Colaco R., Audebert F., Perrone A., and Zocco A. Deposition of NbC thin films by pulsed laser ablation. *Appl. Phys. A*, 69:S569–S571, 1999.

[28] Sansone M., De Bonis A., Santagata A., Rau J. V., Galasso A., and Teghil R. Pulsed laser ablation and deposition of Niobium carbide. *Appl. Surf. Sci.*, 374:112–116, 2016.

[29] Barinov S. M., Ferro D., Bertuli C., and D'Alessio L. Hardness of Hafnium carbide films deposited on silicon by pulsed laser ablation. *J. Mater. Sci. Lett.*, 20:1485–1487, 2001.

[30] Teghil R., De Bonis A., Galasso A., Villiani P., and Santagata A. Femtosecond pulsed laser ablation deposition of Tantalum carbide. *Appl. Surf. Sci.*, 254:1220–1223, 2007.

[31] Santerre F., El Khakani M. A., Chaker M., and Dodelet J. P. Properties of TiC thin films grown by pulsed laser deposition. *Appl. Surf. Sci.*, 148:24–33, 1999.

[32] Craciun V., Craciun D., Howard J. M., and Woo J. Pulsed laser deposition of crystalline ZrC thin films. *Thin Sold Films*, 515:4636–4639, 2017.

[33] Craciun D., Socol G., Dorcioman G., Stefan N., Bourne G., and Craciun V. High quality ZrC, ZrC/ZrN and ZrC/TiN thin films grown by pulsed laser deposition. *J. Optoelectron. Adv. Mater.*, 12(3):461–465, 2010.

[34] Craciun D., Socol G., Stefan N., Mihailescu I. N., Bourne G., and Craciun V. High-repetition rate pulsed laser deposition of ZrC thin films. *Surf. Coat. Tech.*, 203:1055–1058, 2009.

[35] Stafe M., Marcu A., and Puscas N. N. *Pulsed Laser Ablation of Solids: Basics, Theory and Applications*. Springer-Verlag Berlin Heidelberg, 2014.

[36] Amoruso S., Bruzzese R., Spinelli N., and Velotta R. Laser ablation plasmas. *J. Phys. B: At. Mol. Opt. Phys.*, 32:R131–R172, 1999.

[37] Krajewski A., D'Alessio L., and De Maria G. Physiso-Chemical and Thermophysical Properties of Cubic Binary Carbides. *Cryst. Res. Technol.*, 33(3):341–374, 1998.

[38] Sinha S. Thermal model for nanosecond laser ablation of alumina. *Ceram. Int.*, 41:6596–6603, 2015.

[39] Stafe M. Theoretical photo-thermo-hydrodynamic approach to the laser ablation of metals. *J. Appl. Phys.*, 112(123112):1–7, 2012.

[40] Pershin S. M., Lednev V. N., and Bunkin A. F. Laser ablation of alloys: selective evaporation model. *Phys. Wave Phenom.*, 19(4):261–274, 2011.

[41] Sinha S. Thermal model based simulation of nanosecond pulsed laser irradiation of Ti_6Al_4v alloy. *J. Laser Appl*, 31(032008):1–9, 2019.

[42] Sinha S. Nanosecond laser ablation of thoria fuel pellets for microstructural study. *J. Nucl. Mater.*, 396:257–263, 2010.

[43] Bulgakova N. M. and Bulgakov A. V. Pulsed aser ablation of solids: transition from normal vaporisation to phase explosion. *Appl. Phys. A*, 73:199–208, 2001.

[44] Oura K., Lifshits V. G., Saranin A. A., Zotov A. V., and Katayama M. *Surface Science - An Introduction*. Springer-Verlag, 2004.

[45] Harald Friedrich. *Lecture Notes in Physics Volume 872: Scattering Theory*. Springer-Verlag Berlin Heidelberg, 2013.

[46] Moulder J. F., Stickle W. F., Sobol P. E., and Bomben K. D. *Handbook of X-ray Photoelectron Spectroscopy*. Perkin-Elmer Corporation, 1993.

[47] Briggs D. and Grant J. T. *Surface Analysis by Auger and X-ray Photoelectron Spectroscopy.* IM Publications, 2003.

[48] J. J. Yeh. *Atomic Calculation of Photoionization Cross-Sections and Asymmetry Parameters.* Gordon and Breach Science Publishers, 1993.

[49] Yeh J. J. and Lindau I. Atomic subshell photoionization cross sections and asymmetry parameters: $1 \leq z \leq 103$. *At. Data Nucl. Data Tables*, 32(1):1–155, 1993.

[50] Warren B. E. *X-ray Diffraction.* Addison-Wiley, 1969.

[51] The Materials Project. Materials Data on TiC by Materials Project. *doi: 10.17188/1279030.*

[52] The Materials Project. Materials Data on NbC by Materials Project. *doi: 10.17188/1282001.*

[53] The Materials Project. Materials Data on ZrC by Materials Project. *doi: 10.17188/1202103.*

[54] The Materials Project. Materials Data on HfC by Materials Project. *doi: 10.17188/1196352.*

[55] The Materials Project. Materials Data on TaC by Materials Project. *doi: 10.17188/1187404.*

[56] Greczynski G., Primetzhofer D., and Hultman L. Reference binding energies of transition metal carbides by core-level x-ray photoelectron spectroscopy free from Ar^+ etching artefacts. *Appl. Surf. Sci.*